

We are IntechOpen, the world's leading publisher of Open Access books Built by scientists, for scientists

4,800

Open access books available

122,000

International authors and editors

135M

Downloads

Our authors are among the

154

Countries delivered to

TOP 1%

most cited scientists

12.2%

Contributors from top 500 universities



WEB OF SCIENCE™

Selection of our books indexed in the Book Citation Index
in Web of Science™ Core Collection (BKCI)

Interested in publishing with us?
Contact book.department@intechopen.com

Numbers displayed above are based on latest data collected.
For more information visit www.intechopen.com



MRI RF-Induced Heating in Heterogeneous Human Body with Implantable Medical Device

Ran Guo, Jianfeng Zheng and Ji Chen

Additional information is available at the end of the chapter

<http://dx.doi.org/10.5772/intechopen.71384>

Abstract

Magnetic resonance imaging (MRI) radio frequency (RF)-induced heating is one of the most important concerns of MRI safety for patients, especially with orthopaedic healthcare products. In this chapter, numerical modelling and simulations were conducted to study the RF-induced heating within a 1.5T and 3T magnetic resonance (MR) environment. Numerical simulations were firstly conducted to study the difference between the cases of implantable medical devices inside the phantom and the human body. Then, numerical modelling were conducted to describe the difference of electromagnetic behaviours between the homogeneous phantom and heterogeneous human tissues. The MRI RF-induced heating due to an implantable medical device behaves significantly different in homogeneous media and in heterogeneous human body. For typical orthopaedic medical devices, such as healthcare products applied to shoulder, humerus, hip, femur and tibia, the properties of the RF-induced heating are different in general phantom and in human body. The hot spot location, as well as worst case configuration were evaluated and it was found that they were determined by the incident field and electromagnetic properties of medium. With further scaling, the RF-induced heating in human body for the orthopedic devices can be assessed by phantom studies.

Keywords: MRI, RF-induced heating, orthopedic implant, phantom

1. Introduction

Many of the MR-related injuries and the few fatalities that have occurred were the apparent result of failure to follow safety guidelines or of the use of inappropriate information related to the safety aspects of biomedical implants and devices [1–7]. The preservation of a safe MR environment requires constant attention to the care of patients and individuals with

metallic implants and devices, because the variety and complexity of these objects constantly changes [5–7]. Therefore, to guard against accidents in the MR environment, it is important to understand the risk associated with implantable medical devices which may cause potential problems.

The radiofrequency coils could send energy, in the form of electromagnetic radiation, into the human body. Since the energy is in the radio frequency range, the radiation is not ionizing. But it still can influence biological tissue. During MR procedures, the majority of the RF power transmitted for imaging or spectroscopy (especially for carbon decoupling) is transformed into heat within the patient's tissue as a result of resistive losses, through convection, conduction, radiation or evaporation [8–18]. Thus, a potential concern in MRI is the heating of the body during image acquisition.

To evaluate the RF-induced heating, the specific absorption rate (SAR) is applied to determine how much electromagnetic energy is absorbed by the body. SAR is typically expressed in unites of watts per kilogram, or W/kg. So the SAR could be defined as:

$$SAR(r) = \frac{\sigma}{2\rho} E^2(r) \quad (1)$$

where E is the total electric field and σ and ρ are the conductivity and density of biological tissue, respectively. The temperature rise in human body or phantom could be calculated by the total SAR according to the bio heat equation. SAR depends on the pulse sequence and the size, geometry, and conductivity of the absorbing object. To ensure participant safety, SAR in MRI studies is limited to minimize temperature increases.

The first study of human thermal responses to RF radiation-induced heating during an MR procedure was conducted by Schaefer et al. [19]. Temperature changes and other physiological parameters were assessed in volunteer subjects exposed to relatively high, whole-body averaged SARs (approximately 4.0 W/kg). The data indicated that there were no excessive temperature elevations or other deleterious physiological consequences related to the exposure to RF radiation [19].

However, for patients with medical implants, MRI-related RF induced heating is potentially problematic. The evaluation of heating for an implant or device is particularly challenging because of the many factors that affect temperature increase in these items. Variables that impact heating include the following: the specific type of implant or device; the electrical characteristic of the implant or device; the RF wavelength of the MR system; the type of transmit RF coil that is used (i.e., transmit head versus transmit body RF coil); the amount of RF energy delivered (i.e., the specific absorption rate, SAR); the landmark position or body part undergoing MRI relative to the transmit RF coil; and the orientation or configuration of the implant or device relative to the source of transmit RF coil.

In this chapter, it shows the importance of evaluation the MRI-related RF induced heating issues for patient with implantable medical devices. Generally, the estimation and measurement is based on *in-vitro* numerical simulation and experiment. And assessment methods could be separated into active and passive medical implants, respectively, due to the

configuration difference of these devices. With the help of the *in-vitro* evaluation methods, it provides a highly possible way to estimate the temperature increase for patient with implants or devices during MRI examination.

2. *In-vivo* and *in-vitro*

MRI may be contraindicated for a given patient primarily due to its potential risks associated with a metallic implant or device. Although many investigations have been performed using laboratory animals to determine thermoregulatory reactions to tissue heating associated with exposure to RF radiation, these experiments do not directly apply to the conditions that occur during MR procedures, nor can they be extrapolated to provide useful information for various reasons [20, 21]. For example, the pattern of RF absorption or the coupling of radiation to biological tissues is primarily dependent on the organism's size, anatomical features, duration of exposure, sensitivity of the involved tissues (e.g., some tissues are more "thermal sensitive" than others), and a myriad of other variables [14, 21, 22]. Furthermore, there is no laboratory animal that sufficiently mimics or simulates the thermoregulatory responses of an organism with the dimensions and specific responses to that of a human subject. Therefore, experimental results obtained in laboratory animals cannot be simply "scaled" or extrapolated to predict thermoregulatory or other physiological changes in human subjects exposed to RF radiation-induced heating during MR procedures [14, 15, 22], and. In consideration of the above, *in-vitro* testing is performed to assess the various MRI issues for implants and devices in order to properly characterize the possible risks.

One of *in-vitro* methods is to use standard American Society for Testing and Materials (ASTM) phantom. ASTM F2182-11A depicts the guideline to measure the RF heating induced by implanted medical devices in a standard phantom filled with gelled-saline which mimic the muscles [23]. Studies have been conducted to evaluate the RF heating induced by orthopedic implants. Commonly a phantom or homogenous media is used to mimic the environments as the implants locate in human body in experiments and/or numerical simulations [24–32].

Although the RF-induced heating evaluating method using the phantom filled with gelled-saline is widely used, it is obvious that the RF environment of a human body and a phantom filled with gelled-saline are quite different. The power deposition due to an implant for a given incident RF field is a function of the physical properties of the implant and electrical properties of the surrounding medium. Compared with homogeneous gelled-saline in phantom, human body is an inhomogeneous circumstance which includes different tissues with various permittivity and conductivity in a wide range. Hence, it is necessary to study a feasible guide with *in-vitro* phantom to assess the RF-induced heating in heterogeneous human body.

2.1. Human body: heterogeneous medium

With the development of computational electromagnetics, anatomical computer models of the human body have been used for nearly four decades for dosimetric applications in electromagnetics (EM) [33] and in medical radiation physics [34]. The most prominent numerical

Name	Age (years)	Gender	Height (m)	Mass (kg)	BMI (kg/m ²)
Duke	34	Male	1.74	70	23.1

Table 1. The characteristics of the anatomical Duke model.

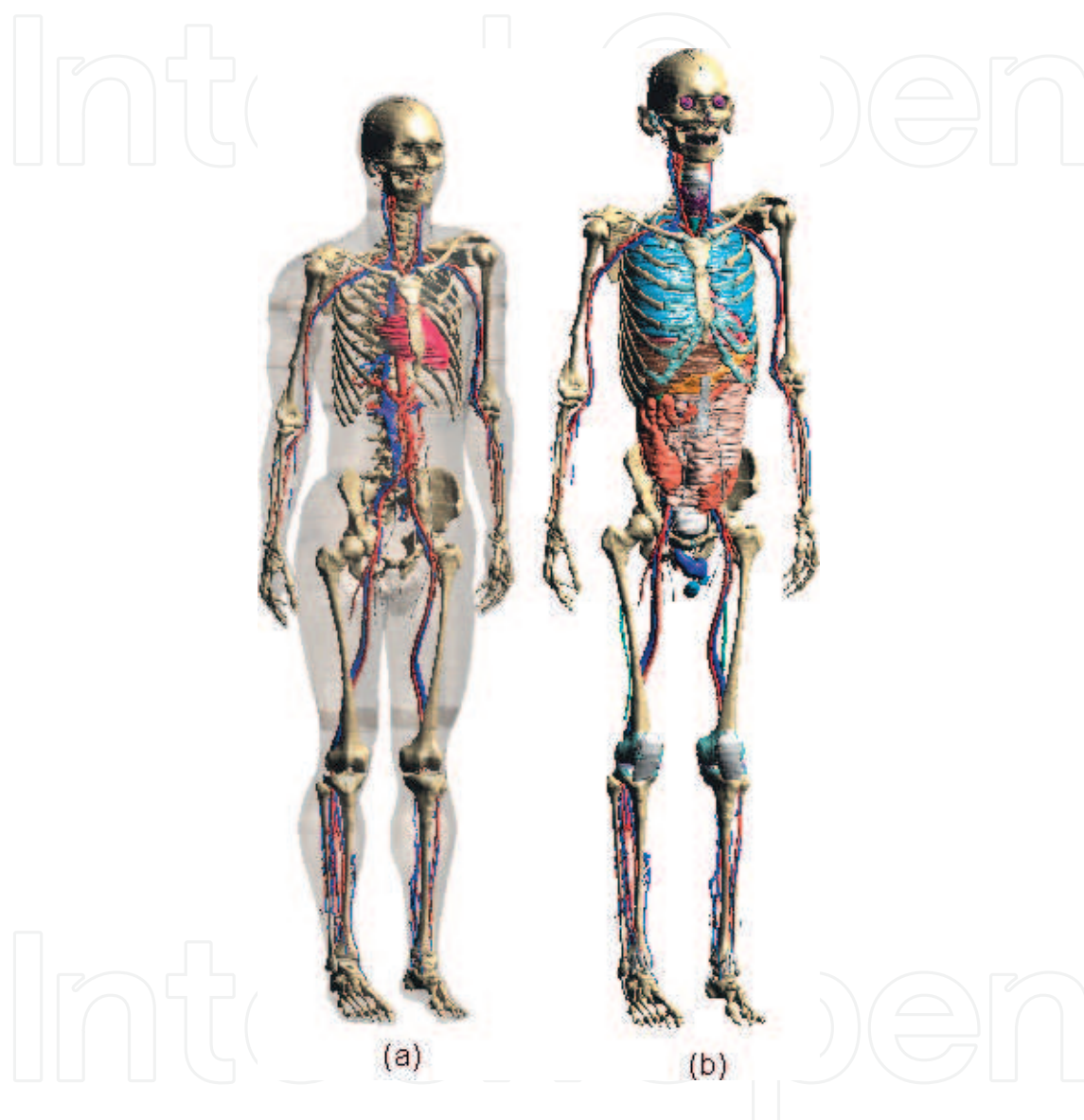


Figure 1. The segmented tissues and organs of anatomic body.

methods used in computational dosimetry of electromagnetic fields are based on finite-difference formulations of the underlying differential equations. For the simulation of both RF fields and induced tissue heating, the finite-difference time-domain (FDTD) method in its formulations by Yee [35] and Patankar [36] is applied to rectilinear grids to optimally handle large voxel models. The reconstructed human model used in this Chapter is from the Virtual Family [37]. It is based on high resolution magnetic resonance images of healthy volunteers. Seventy seven different tissue types were distinguished during the segmentation. Currently,

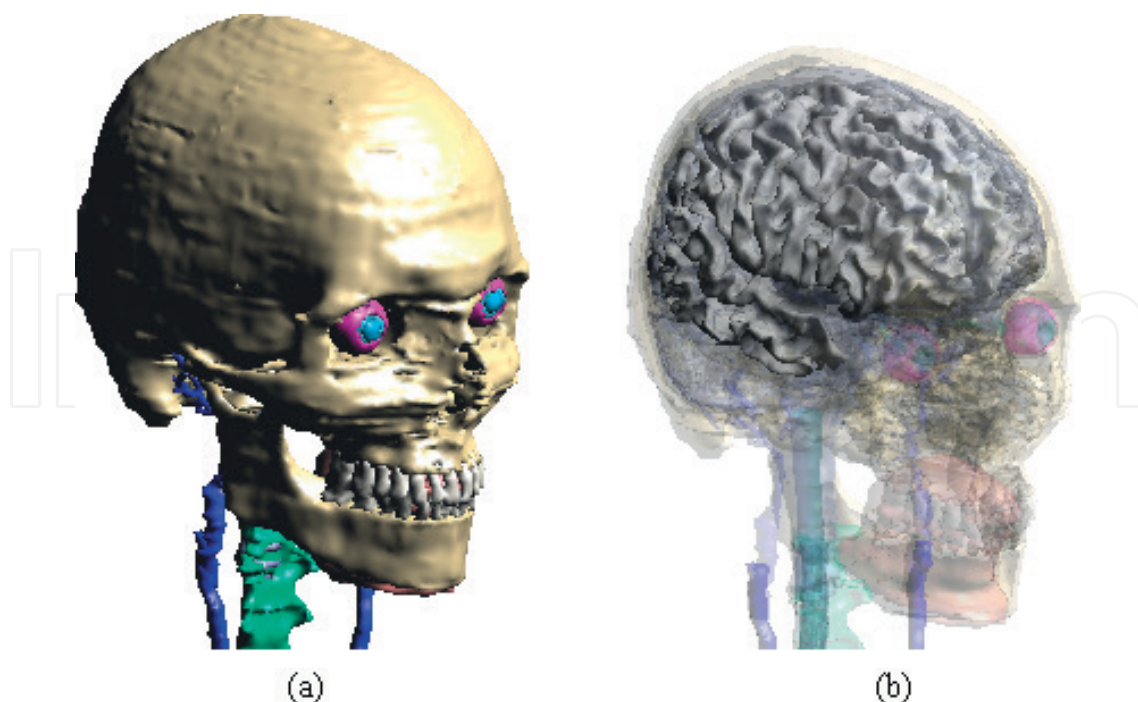


Figure 2. The segmented tissues and organs of anatomic brain.

Tissue or organ	Electric conductivity (S/m)		Relative permittivity		Density (kg/m ³)
	1.5 T/64 MHz	3 T/128 MHz	1.5 T/64 MHz	3 T/128 MHz	
Adrenal gland	0.778305	0.804166	73.9472	66.7839	1027.5
Air internal	0	0	1	1	1.2
Artery	1.20667	1.24863	86.4441	73.159	1049.75
Bladder	0.287352	0.298014	24.5943	21.8607	1035
Blood vessel	1.20667	1.24863	86.4441	73.159	1049.75
Bone	0.0595255	0.0673524	16.6812	14.7171	1908
Brain gray matter	0.510868	0.58673	97.4294	73.5204	1044.5
Brain white matter	0.291504	0.342151	67.8358	52.5338	1041
Bronchi	0.528415	0.559346	58.8896	50.5714	1101.5
Bronchi lumen	0	0	1	1	1.2
Cartilage	0.452103	0.488375	62.9145	52.9242	1099.5
Cerebellum	0.719003	0.829397	116.35	79.7377	1045
Cerebrospinal fluid	2.06597	2.14301	97.3124	84.0406	1007
Commissure anterior	0.291504	0.342151	67.8358	52.5338	1041
Commissure posterior	0.291504	0.342151	67.8358	52.5338	1041
Connective tissue	0.474331	0.498727	59.4892	51.8568	1525
Cornea	1.00058	1.05874	87.3779	71.4566	1050.5

Tissue or organ	Electric conductivity (S/m)		Relative permittivity		Density (kg/m ³)
	1.5 T/64 MHz	3 T/128 MHz	1.5 T/64 MHz	3 T/128 MHz	
Diaphragm	0.688213	0.719235	72.2347	63.4948	1090.4
Ear cartilage	0.452103	0.488375	62.9145	52.9242	1099.5
Ear skin	0.43575	0.522704	92.1679	65.437	1109
Epididymis	0.884871	0.926404	84.5272	72.1279	1082
Esophagus	0.877842	0.912807	85.8204	74.895	1040
Esophagus lumen	0	0	1	1	1.2
Eye lens	0.28588	0.312684	50.3392	42.7911	1075.5
Eye sclera	0.882673	0.917665	75.2998	64.9991	1032
Eye vitreous humor	1.50315	1.50536	69.1264	69.0619	1004.5
Fat	0.0661558	0.0697299	13.6436	12.3711	911
Gall bladder	1.48179	1.5764	105.443	88.8995	928
Heart lumen	1.20667	1.24863	86.4441	73.159	1049.75
Heart muscle	0.678423	0.766108	106.514	84.2573	1080.8
Hippocampus	0.510868	0.58673	97.4294	73.5204	1044.5
Hypophysis	0.778305	0.804166	73.9472	66.7839	1053
Hypothalamus	0.778305	0.804166	73.9472	66.7839	1053
Intervertebral disc	0.452103	0.488375	62.9145	52.9242	1099.5
Kidney cortex	0.741316	0.852313	118.556	89.6168	1049
Kidney medulla	0.741316	0.852313	118.556	89.6168	1044
Large intestine	0.638152	0.705214	94.6639	76.5722	1088
Large intestine lumen	0.688213	0.719235	72.2347	63.4948	1045.2
Larynx	0.452103	0.488375	62.9145	52.9242	1099.5
Liver	0.447984	0.510897	80.5595	64.2507	1078.75
Lung	0.288977	0.315616	37.1022	29.4677	394
Mandible	0.0595255	0.0673524	16.6812	14.7171	1908
Marrow	0.154335	0.162021	16.4355	13.5377	1028.5
Medulla oblongata	0.719003	0.829397	116.35	79.7377	1045.5
Meniscus	0.452103	0.488375	62.9145	52.9242	1099.5
Midbrain	0.719003	0.829397	116.35	79.7377	1045.5
Mucosa	0.488039	0.544202	76.7233	61.5852	1102
Muscle	0.688213	0.719235	72.2347	63.4948	1090.4
Nerve	0.312174	0.353802	55.0621	44.0653	1075
Pancreas	0.778305	0.804166	73.9472	66.7839	1086.5
Patella	0.0595255	0.0673524	16.6812	14.7171	1908

Tissue or organ	Electric conductivity (S/m)		Relative permittivity		Density (kg/m ³)
	1.5 T/64 MHz	3 T/128 MHz	1.5 T/64 MHz	3 T/128 MHz	
Penis	0.429311	0.478934	68.6368	55.9888	1101.5
Pharynx	0	0	1	1	1.2
Pineal body	0.778305	0.804166	73.9472	66.7839	1053
Pons	0.719003	0.829397	116.35	79.7377	1045.5
Prostate	0.884871	0.926404	84.5272	72.1279	1045
SAT	0.0661558	0.0697299	13.6436	12.3711	911
Skin	0.43575	0.522704	92.1679	65.437	1109
Skull	0.0595255	0.0673524	16.6812	14.7171	1908
Small intestine	1.59145	1.69285	118.363	87.9725	1030
Small intestine lumen	0.688213	0.719235	72.2347	63.4948	1045.2
Spinal cord	0.312174	0.353802	55.0621	44.0653	1075
Spleen	0.743914	0.835186	110.559	82.8917	1089
Stomach	0.877842	0.912807	85.8204	74.895	1088
Stomach lumen	0.688213	0.719235	72.2347	63.4948	1045.2
Teeth	0.0595255	0.0673524	16.6812	14.7171	2180
Tendon ligament	0.474331	0.498727	59.4892	51.8568	1142
Testis	0.884871	0.926404	84.5272	72.1279	1082
Thalamus	0.510868	0.58673	97.4294	73.5204	1044.5
Thymus	0.778305	0.804166	73.9472	66.7839	1023
Thyroid gland	0.778305	0.804166	73.9472	66.7839	1050
Tongue	0.652145	0.687137	75.2998	64.9991	1090.4
Trachea	0.528415	0.559346	58.8896	50.5714	1080
Trachea lumen	0	0	1	1	1.2
Ureter Urethra	0.429311	0.478934	68.6368	55.9888	1101.5
Vein	1.20667	1.24863	86.4441	73.159	1049.75
Vertebrae	0.0595255	0.0673524	16.6812	14.7171	1908

Table 2. The electromagnetic properties of the segmented tissues and organs.

the models are being widely applied in several studies on electromagnetic exposure, device optimization and medical applications. **Table 1** shows the characteristics of the anatomical model. Duke model is an anatomical model of adult male which is shown in **Figures 1** and **2**. And **Table 2** shows the segmented tissues and organs of the model, as well as the electromagnetic properties.

2.2. ASTM phantom: *in-vitro* measurement

The standard F2182 describe a test method for measurement of RF induced heating on or near passive implants and its surrounding during MRI procedure. A design of phantom container is introduced in the standard with its dimension shown in **Figure 3**. The material of phantom container are electrical insulators and non-magnetic and non-metallic. The phantom container is filled with a gelled-saline which has a relative permittivity $\epsilon_r = 80.4$ and conductivity of $\sigma = 0.47$ S/m. In order to have a great conductivity and viscosity, a suitable gelled saline should be made with 1.32 g/L NaCl and 10 g/L polyacrylic acid (PAA) in water. Numerical simulations indicate that the maximum electric field inside the ASTM phantom is at mid-axial plane about 2 cm away from the vertical phantom side wall. To maximize the heating, and thereby maximizing the signal-to-noise ratio, we placed the implants at this location.

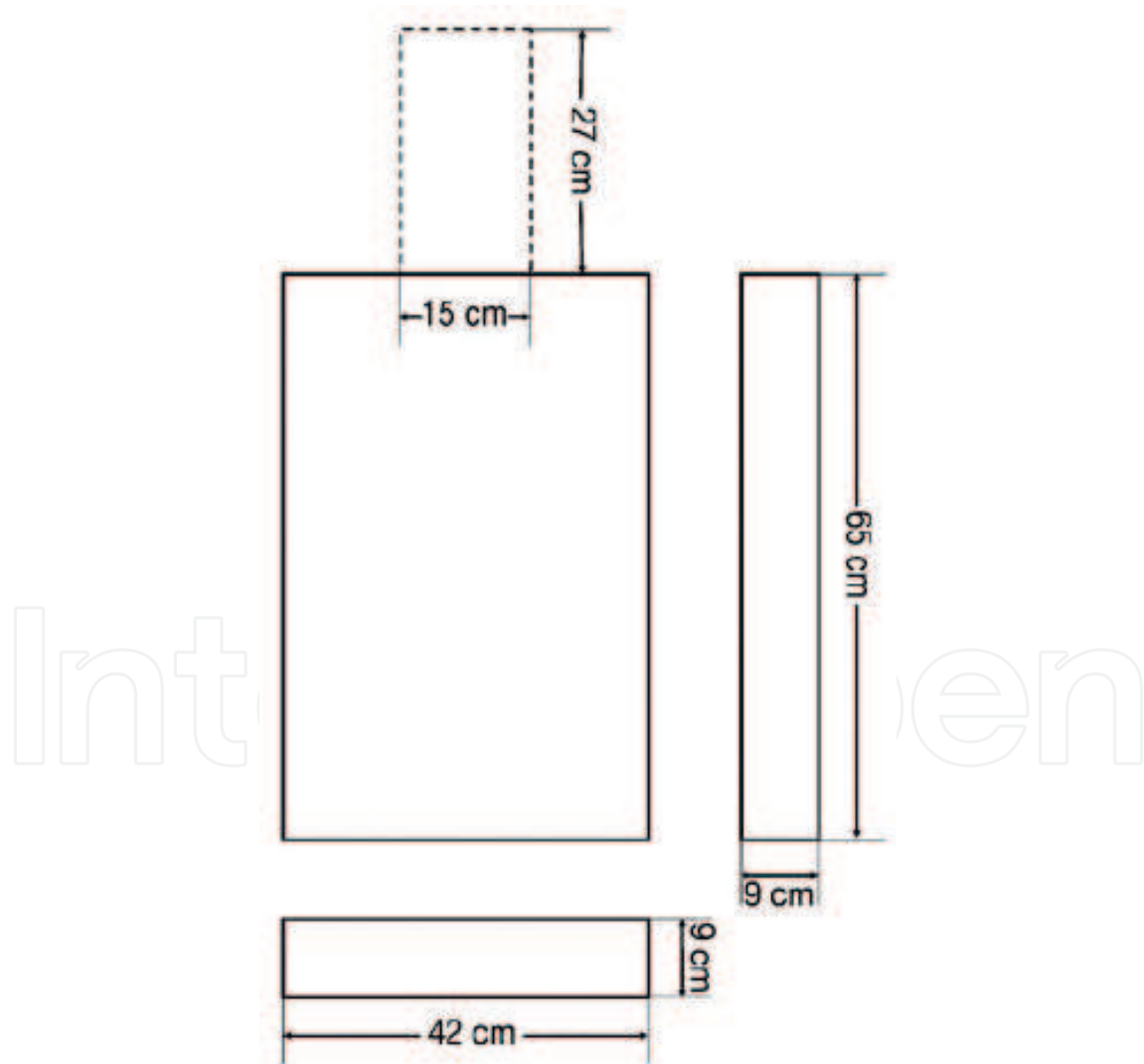


Figure 3. The structure and dimension of standard ASTM phantom.

A generic RF transmit body coil is developed and shown in **Figure 4**. The upper plots represent a 1.5 T RF coil and the lower two plots represent a 3 T RF coil. A physical coil is usually difficult to model and it takes much longer simulation time to reach the steady state of the simulation. It has been shown that using a non-physical coil could significantly reduce the simulation time while providing the same result as that from a physical coil. Thus, rather than modeling the exact physical coil, the non-physical coils were modeled in this study. The two coils have the same dimensions, and both have 8 rungs. The diameter of the RF coil is 63 cm, and the height of the RF coil is 65 cm. The eight parallel lines or the rungs are one dimensional line current excitation. The end rings on top and bottom of the RF coils are tuning capacitors which are also modelled as one dimensional line segments.

The capacitance value is determined from several broadband simulations so that the second highest resonant frequency was adjusted to 64 MHz for 1.5-T and 128 MHz for 3-T systems. The detailed steps are: set an initial capacitance value for all capacitors on end rings and add a broadband pulse signal on one single rung. The other seven rungs are modeled as zero ohm resistors. After the simulation is finished, the power spectrum is extracted. If the second highest resonant frequency is not at appropriate resonant frequencies, the capacitance needs to be adjusted. From this study, the capacitance for the end ring tuning capacitor values is 7.2 pF for 1.5-T RF coil and 1.3 pF for 3-T RF coil.

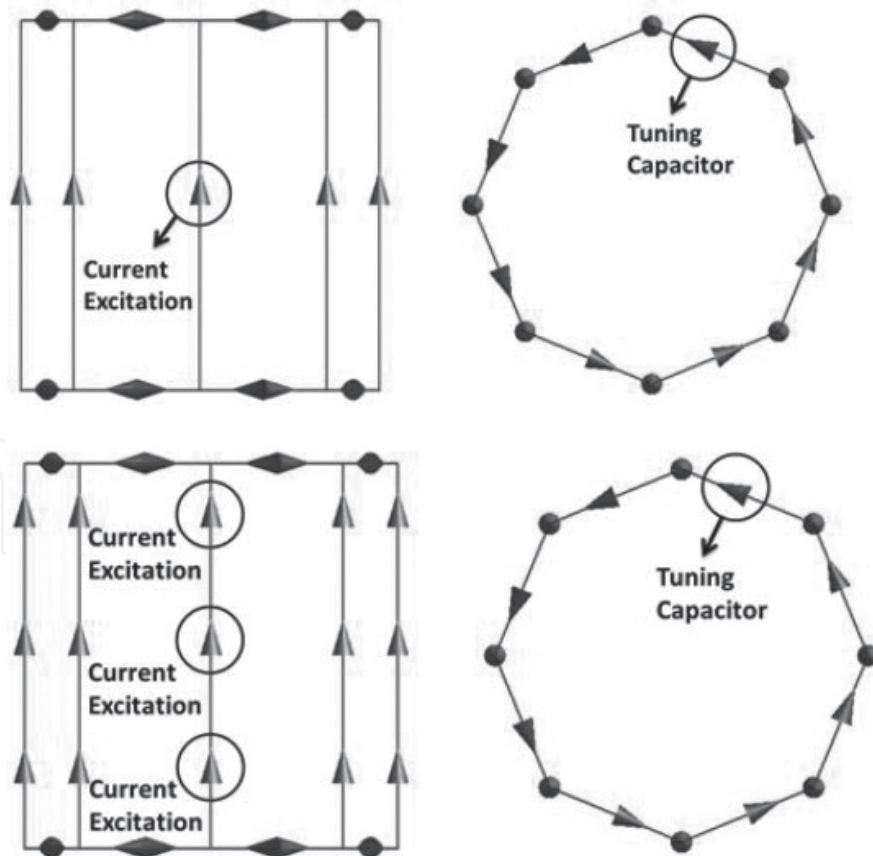


Figure 4. The generic coil model of 1.5-T RF coil (top) and 3-T RF coil (bottom) in SEMCAD X.

3. Passive implantable medical device

Any device intended to be totally or partially introduced into the human body through surgical intervention and intended to remain in place after the procedure for at a long-term duration is considered as an implantable device. Passive devices in terms of their form of operation can be classified as device used for transportation and storage of pharmaceutical liquid, device for alteration of blood, body fluids, medical dressing, surgical instruments; reusable surgical instruments, disposable aseptic device, implantable device, device for contraception and birth control, device for sterilization and cleaning, patient care device, in vitro diagnostic reagent, as well as other passive contacting device or passive supplementary device.

In this chapter, three typical categories of orthopedic implantable devices, bone plate system, hip prostheses and tibia intramedullary nails, are selected for MRI related RF induced heating study which are shown in **Figures 5–7**. The configuration of each implantable device is shown

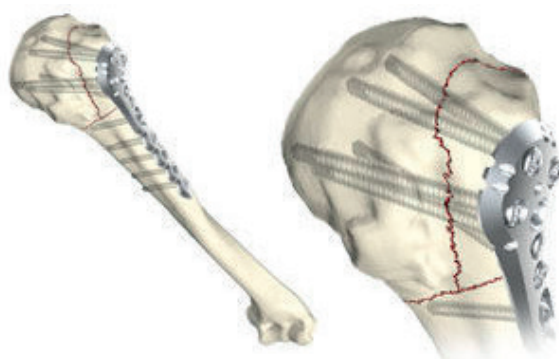


Figure 5. The bone plant system of AxSOS system from Stryker®.



Figure 6. The hip prostheses of Excia® T from Aesculap®.



Figure 7. The tibia intramedullary nails of PROtect™ from Depuy Synthes.

in figure. For bone fragment compression plate, it is designed to offer multiple compression and reconstruction plating options for the treatment of bone fractures. The application of hip prostheses is related to hip revision and arthroplasty. As for intramedullary nails, they are characterized by the anatomic shape, which is intended to replicate the natural anatomic shape of the bones. They have been designed to help restore the shape of the bone and treat the fractured bones.

4. Numerically evaluate RF-induced heating

4.1. FDTD method

In this numerical investigation, we use the finite difference time domain (FDTD) based SEMCAD X 14.8 (SPEAG) simulation platform. Graphics processing unit (GPU) hardware acceleration was achieved using the SPEAG CUDA library with Tesla C2075 graphic card which is can handle up to 90 million cells. To assure convergence of the numerical simulations, the simulation time was set to 20 periods for each simulation. Additionally, the convergence was checked after the simulations were finished. The material of orthopedic devices is set to perfect electric conductor (PEC), and all the numerical results are normalized to a whole body average SAR of 2 W/kg. The SAR distribution is studied for each case.

4.2. Bone plate system

To ensure a comprehensive comparison, the 1g local average peak SAR value at device is extracted for each configuration of femur and humerus system. **Tables 3** and **4** show the value for femur and humerus system. For each numerical result, whole-body average SAR is normalized to 2 W/kg. Since the interaction between RF induced field and implant is dependent on the physical structure of device, the heating effect variations related to the length of plate and screw are studied separately. For femur system, the plate length varies from 100 to 300 mm, and the screw length changes from 10 to 32 mm. For humerus system, the screw dimension is the same as femur system. But the plate length varies only from 100 to 250 mm due to the limit of bone structure. The plate length is studied at first for minimum and maximum screw length. Then the screw length is investigated under the worst case of plate length study which has the highest 1g average peak SAR value for *in-vivo* simulation. **Figures 8–13** show the results which are corresponding to femur and humerus plate system. The solid and dash curve and indicate the *in-vivo* and *in-vitro* results, respectively.

Plate length (mm)		Screw length (mm)	1.5 T/64 MHz		3 T/128 MHz	
			<i>In-vivo</i> SAR _{1g} (W/kg)	<i>In-vitro</i> SAR _{1g} (W/kg)	<i>In-vivo</i> SAR _{1g} (W/kg)	<i>In-vitro</i> SAR _{1g} (W/kg)
100		10	64.20	125.97	79.75	80.90
150		10	94.82	178.62	74.52	64.01
175		10	107.00	190.44	68.50	50.20
200		10	116.65	188.87	63.37	44.69
225		10	117.00	185.04	63.10	37.72
250		10	123.00	169.75	61.23	37.27
275		10	117.00	149.81	53.80	35.33
300		10	105.00	134.91	42.37	38.53
100		32	85.02	100.22	88.26	71.90
150		32	108.17	135.90	55.48	47.74
200		32	104.91	140.27	51.56	41.59
250		32	111.73	123.17	48.94	37.09
300		32	79.94	128.93	27.77	40.70
250(1.5 T)	100(3 T)	15	120.00	150.91	79.30	72.19
250(1.5 T)	100(3 T)	20	121.00	135.71	76.20	68.00
250(1.5 T)	100(3 T)	25	123.00	132.15	64.2	66.52

Table 3. Peak 1g averaged SAR of femur system for *in-vivo* and *in-vitro* cases.

Plate length (mm)	Screw length (mm)	1.5 T/64 MHz		3 T/128 MHz	
		<i>In-vivo</i> SAR _{1g} (W/kg)	<i>In-vitro</i> SAR _{1g} (W/kg)	<i>In-vivo</i> SAR _{1g} (W/kg)	<i>In-vitro</i> SAR _{1g} (W/kg)
100	10	38.02	135.61	65.47	90.51
150	10	63.74	192.14	94.68	59.90
200	10	69.47	204.57	81.84	45.54
250	10	104.57	193.61	86.73	41.50
100	32	30.70	92.17	63.46	64.6
150	32	54.10	124.76	85.39	53.70
200	32	55.90	161.97	75.19	43.39
250	32	109.00	156.38	108.92	42.51
250	15	95.53	161.64	77.82	35.33
250	20	91.02	163.55	72.91	38.94
250	25	88.27	164.54	68.40	41.32

Table 4. The peak 1g average SAR value of humerus system for *in-vivo* and *in-vitro* cases.

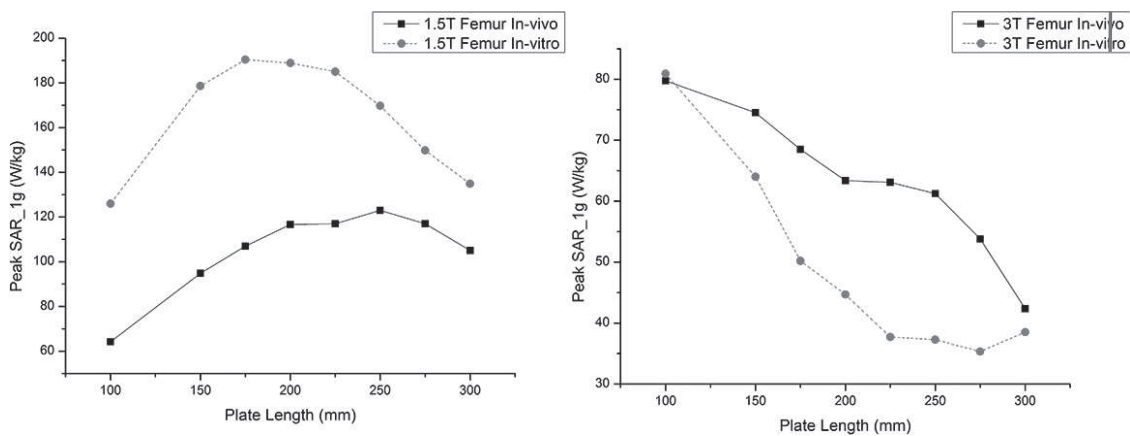


Figure 8. The femur bone plate length study of 10 mm screw for 1.5 T (left) and 3 T (right).

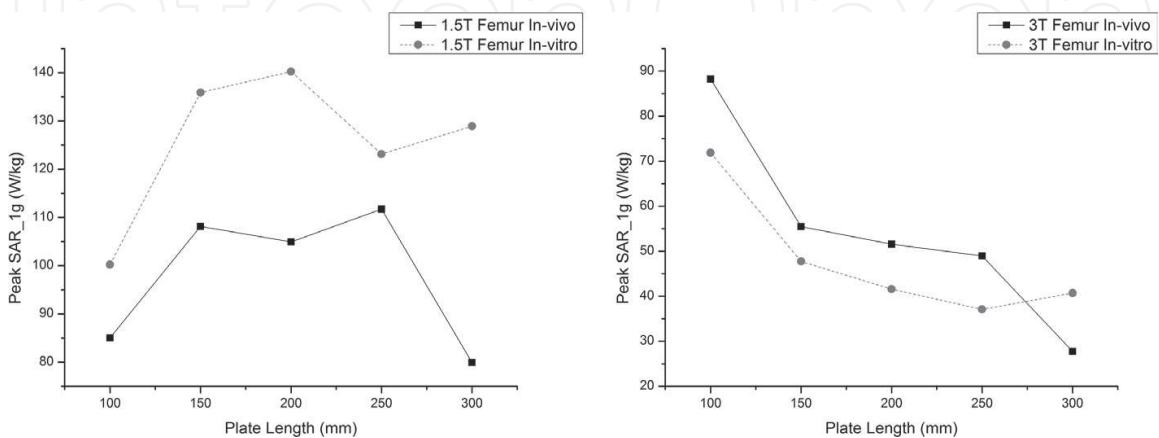


Figure 9. The femur bone plate length study of 32 mm screw for 1.5 T (left) and 3 T (right).

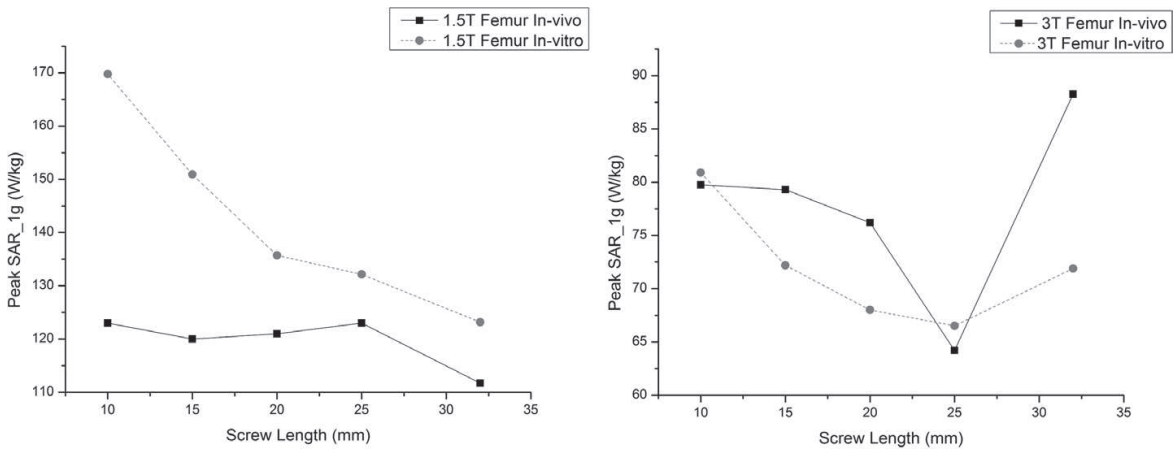


Figure 10. The femur screw length study for 1.5 T (left) and 3 T (right).

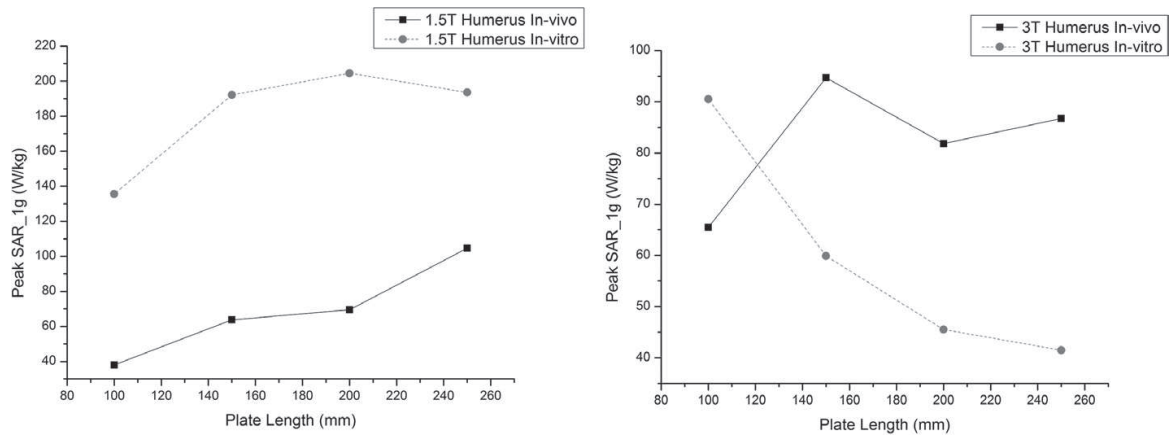


Figure 11. The humerus bone plate length study of 10 mm screw for 1.5 T (left) and 3 T (right).

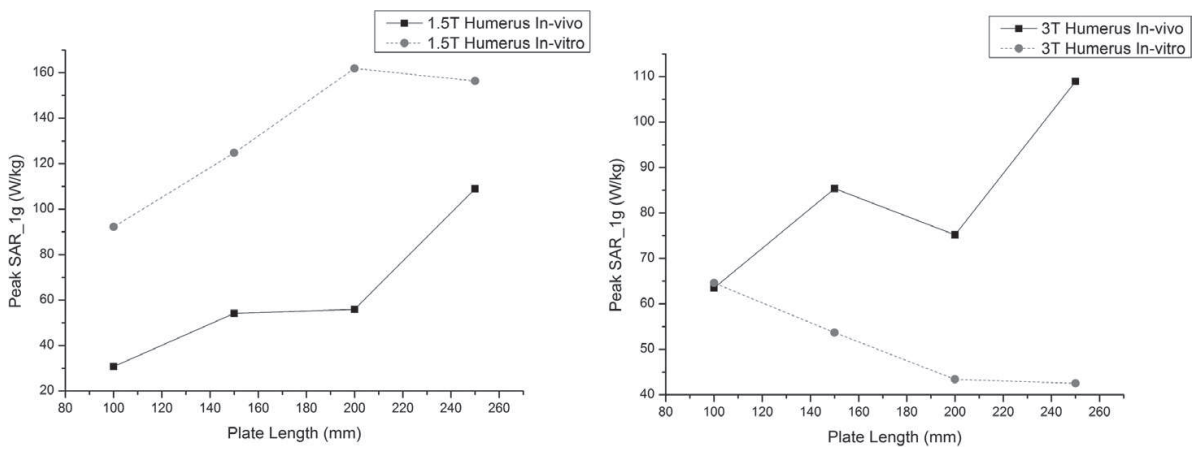


Figure 12. The humerus bone plate length study of 32 mm screw for 1.5 T (left) and 3 T (right).

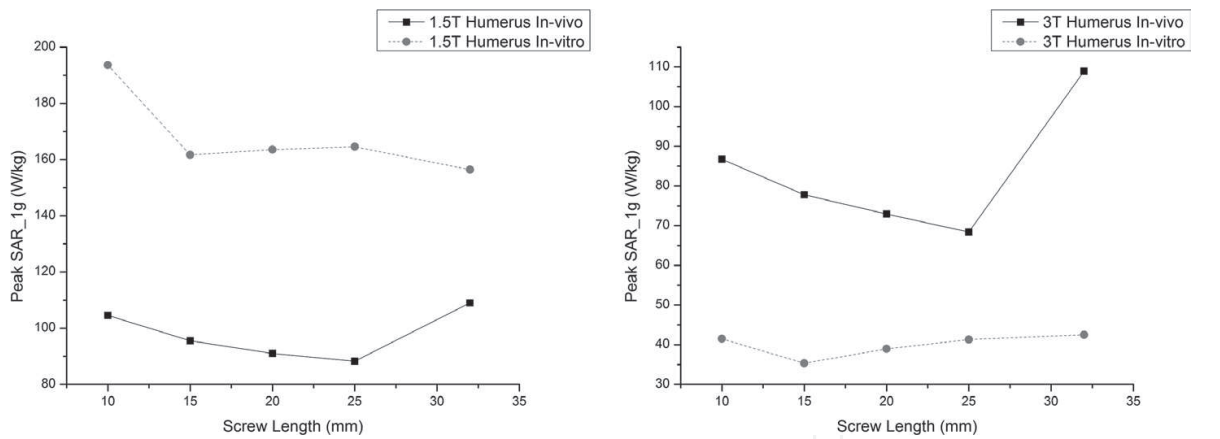


Figure 13. The humerus screw length study for 1.5 T (left) and 3 T (right).

4.3. Hip prostheses

For hip prostheses, the 1g average local peak SAR value at device is also extracted for each configuration. Table 5 shows the value for hip system of various dimensions. The height of hip prostheses stem ranges from 100 to 170 mm. For *in-vivo* simulation, the stem is inserted into the bone marrow. And for the trochanter region, the hip prostheses is touching with soft tissue and muscle. Figure 14 represents the results of hip prostheses. The solid and dash curve and indicate the *in-vivo* and *in-vitro* results, respectively.

4.4. Tibia intramedullary nails

The 1g average local peak SAR value at device is also extracted for each configuration of tibia intramedullary nails. The length of stem ranges from 255 to 360 mm. The entire nail

Stem height (mm)	1.5 T/64 MHz		3 T/128 MHz	
	<i>In-vivo</i> SAR _{1g} (W/kg)	<i>In-vitro</i> SAR _{1g} (W/kg)	<i>In-vivo</i> SAR _{1g} (W/kg)	<i>In-vitro</i> SAR _{1g} (W/kg)
100	83.2764	270.843	43.4746	55.4143
110	81.5782	260.502	35.8247	56.3111
120	77.8568	248.116	24.4627	57.0498
130	74.9259	247.635	21.9093	60.352
140	64.5142	237.51	16.3059	61.7026
150	62.8772	205.328	13.1482	63.2055
160	59.6273	221.781	11.5599	63.9114
170	55.0469	213.602	11.1877	63.8915

Table 5. Peak 1g average SAR of hip prostheses system for *in-vivo* and *in-vitro* cases.

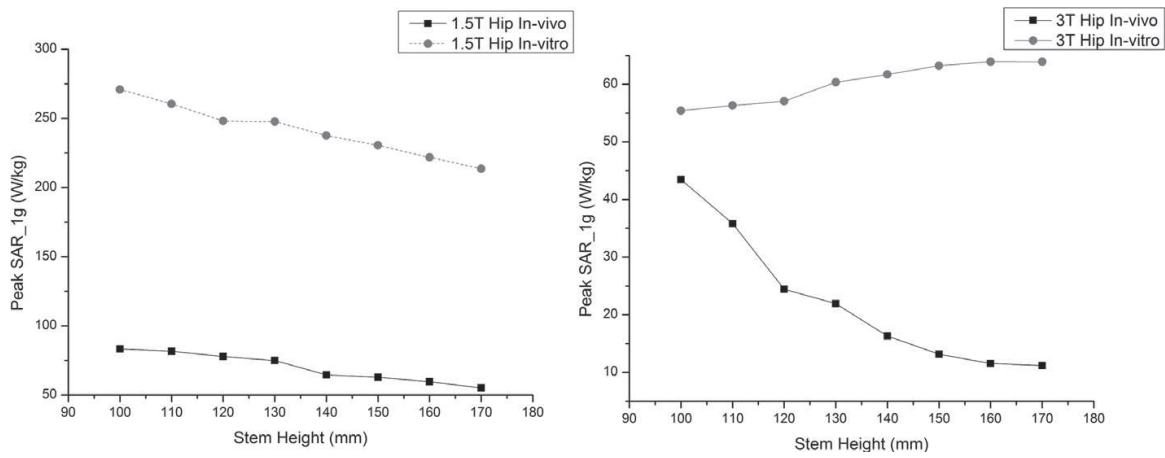


Figure 14. The hip prostheses stem length study for 1.5 T (left) and 3 T (right).

Nail length (mm)	1.5 T/64 MHz		3 T/128 MHz	
	<i>In-vivo</i> SAR _{1g} (W/kg)	<i>In-vitro</i> SAR _{1g} (W/kg)	<i>In-vivo</i> SAR _{1g} (W/kg)	<i>In-vitro</i> SAR _{1g} (W/kg)
255	77.6968	136.331	93.5532	55.4068
270	77.6346	129.249	93.2341	53.6038
285	78.9892	122.28	89.1767	49.8946
300	82.6751	115.745	91.5648	46.8385
315	81.7577	109.28	92.7346	44.0529
330	74.7444	103.319	88.9989	41.6544
345	66.6095	97.3232	90.7795	39.3275
360	67.3469	91.8168	90.1809	37.1875

Table 6. Peak 1g average SAR of tibia nails system for *in-vivo* and *in-vitro* cases.

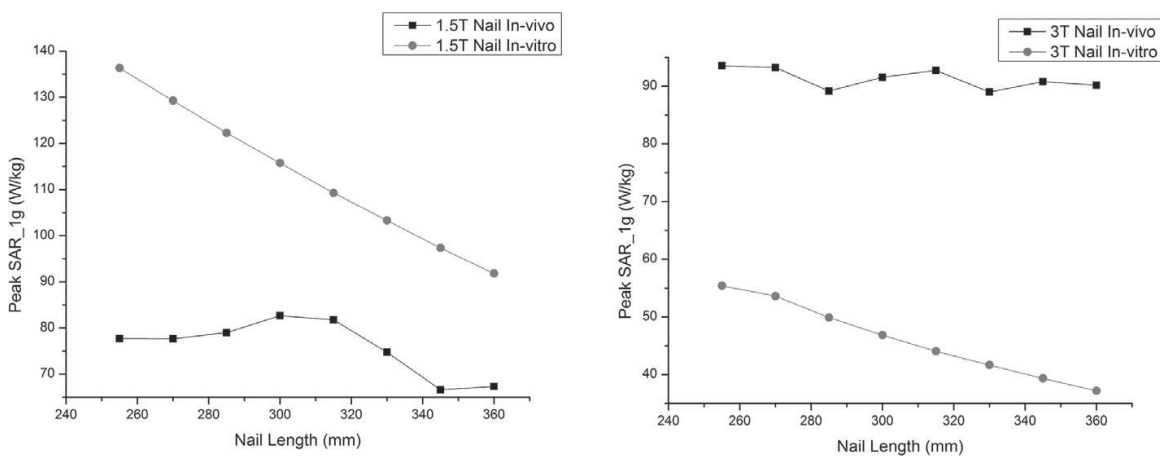


Figure 15. The nail length study for 1.5 T (left) and 3 T (right).

is penetrated into the bone marrow. The four screws are inserted perpendicularly through the nail and bone. **Table 6** shows the value for nail system of various dimensions. **Figure 15** represents the results of tibia intramedullary nails. The solid and dash curve and indicate the *in-vivo* and *in-vitro* results, respectively.

5. Summary

From the comparison between *in-vitro* and *in-vivo* simulations, the RF-induced heating are different because of the variance of incident electric field and surrounding medium. For incident field study, the antenna resonance effect would mainly lead to a heating issue for both *in-vitro* and *in-vivo* situation. Although the wavelength of human muscle and gelled-saline nearly equals to each other, due to the variance of incident RF field, the device dimension causing the resonance would be different. Hence, the trend of peak 1g average SAR value along with plate length is unlike from *in-vitro* to *in-vivo* circumstance. Additionally, when the screw is inserted across the human bone into the muscle, a huge amount of power would dissipated to the human tissue through the screw tip so that induce a large peak SAR value.

Based on the comparison result, conservatively, the *in-vitro* method, such as ASTM phantom, could be used to assess RF-induced heating. However, to accurately assess the RF-induced heating in heterogeneous human body with implantable medical device, due to the limit of homogeneous ASTM phantom, it still needs some improvement to handle several particular cases, especially, when the implantable device is penetrating through various human tissues and organs.

Disclaimer

The mention of commercial products, their sources, or their use in connection with material reported herein is not to be construed as either an actual or implied endorsement of such products by the Department of Health and Human Services.

Author details

Ran Guo, Jianfeng Zheng* and Ji Chen

*Address all correspondence to: jzheng4@central.uh.edu

Department of Electrical and Computer Engineering, University of Houston, Houston, Texas, United States

References

- [1] Schenck JF. Health effects and safety of static magnetic fields. In: Shellock FG, editor. *Magnetic Resonance Procedures: Health Effects and Safety*. Boca Raton, FL: CRC; 2001. p. 1-30
- [2] Zaremba LA. FDA guidance for magnetic resonance system safety and patient exposures: Current status and future considerations. In: Shellock FG, editor. *Magnetic Resonance Procedures: Health Effects and Safety*. Boca Raton, FL: CRC; 2001. p. 183-196
- [3] U.S. Food and Drug Administration, Center for Devices and Radiological Health. MDR Data Files. Available at: www.fda.gov/CDRH/mdrfile.html. [Accessed: April 1, 2003]
- [4] U.S. Food and Drug Administration, Center for Devices and Radiological Health. Manufacturer and User Facility Device Experience Database (MAUDE): File Formats for FOI Releasable Data. Available at: www.fda.gov/cdrh/maude.html
- [5] Shellock FG. *Reference Manual for Magnetic Resonance Safety, Implants, and Devices: 2004 Edition*. Los Angeles, CA: Biomedical Research Publishing; 2004
- [6] Shellock FG. *Pocket Guide to MR Procedures and Metallic Objects: Update 2001*. Philadelphia, PA: Lippincott Williams & Wilkins; 2001
- [7] Shellock FG. *Magnetic Resonance Procedure: Health Effects and Safety*. Boca Raton, FL: CRC; 2001
- [8] Edelman RR, Shellock FG, Ahladis J, Practical MRI. For the technologist and imaging specialist. In: Edelman RR, Hesselink J, editors. *Clinical Magnetic Resonance*. Philadelphia: WB Saunders; 1990. p. 80-115
- [9] Persson BRR, Stahlberg F. *Health and Safety of Clinical NMR Examinations*. Boca Raton, FL: CRC Press; 1989. p. 59-79
- [10] Shellock FG, Kanal E. *Magnetic Resonance: Bio Effects, Safety, and Patient Management*. 2nd ed. New York: Lippincott-Raven; 1996. p. 25-48
- [11] Shellock FG. Biological effects and safety aspects of magnetic resonance imaging. *Magnetic Resonance Quarterly*. 1989;5:243-261
- [12] Kanal E, Shellock FG, Talagala L. Safety considerations in MR imaging. *Radiology*. 1990; 176:593-606
- [13] Morvan D, Leroy-Willig A, Jehenson P, Cuenod CA, Syrota A. Temperature changes induced in human muscle by radiofrequency H-1 coupling: Measurement with an MR imaging diffusion technique. *Radiology*. 1992;185:871-874
- [14] Shellock FG. MRI Bioeffects and safety. In: Atlas S, editor. *Magnetic Resonance Imaging of the Brain and Spine*. New York: Raven Press; 1990
- [15] Shellock FG. Thermal responses in human subjects exposed to magnetic resonance imaging. *Annals of the New York Academy of Sciences*. 1992:260-272

- [16] Bottomley PA, Redington RW, Edelstein WA, et al. Estimating radiofrequency power deposition in body NMR imaging. *Magnetic Resonance in Medicine*. 1985;**2**:336-349
- [17] Bottomley PA, Edelstein WA. Power deposition in whole body NMR imaging. *Medical Physics*. 1981;**8**:510-512
- [18] Shellock FG. Magnetic resonance imaging: bioeffects, safety, and patient management [J]. *Reviews of Magnetic Resonance in Medicine*. 1992;**4**:21-63
- [19] Schaefer DJ, Barber BJ, Gordon CJ, et al. Thermal effects of magnetic resonance imaging. In: *Book of Abstracts, Society for Magnetic Resonance in Medicine*. Vol. 2. Berkeley, CA: Society for Magnetic Resonance in Medicine. 1985. p. 925
- [20] Gordon CJ. Thermal physiology. In: *Biological Effects of Radiofrequency Radiation*. Washington, DC: EPA-600/8-83-026A; 1984 P 4-1-4-28
- [21] Gordon CJ. Effect of radiofrequency radiation exposure on thermoregulation. *ISI Atlas of Science, Animal and Plant Sciences*. 1988;**1**:245-250
- [22] Gordon CJ. Normalizing the thermal effects of radiofrequency radiation: Body mass versus total body surface area. *Bioelectromagnetics*. 1987;**8**:111-118
- [23] ASTM International: Standard Test Method for Measurement of radio frequency induced heating near passive implants during magnetic resonance imaging ASTM Standard F2182-11. ASTM International: West Conshohocken, PA; 2011 www.astm.org
- [24] Powell J, Papadaki A, Hand J, Hart A, McRobbie D. Numerical simulation of SAR induced around Co-Cr-Mo hip prostheses in situ expose to RF fields associated with 1.5 and 3 T MR body coils. *Magnetic Resonance in Medicine*. 2012;**68**:960-968
- [25] Liu Y, Chen J, Shellock FG, et al. Computational and experimental studies of an orthopedic implant: MRI-related heating at 1.5-T/64-MHz and 3-T/128-MHz. *Journal of Magnetic Resonance Imaging*. 2013;**37**(2):491-497
- [26] Liu Y, Shen J, Kainz W, et al. Numerical investigations of MRI RF field induced heating for external fixation devices. *Biomedical Engineering Online*. 2013;**12**(1):12
- [27] Guo R, Zheng J, Chen J, et al. RF-induced heating comparison between *in-vivo* and in-phantom for 1.5 T MRI. *Electromagnetic compatibility (EMC), 2016 IEEE International Symposium on IEEE*, 2016: 121-125
- [28] Mohsin SA, Sheikh NM, Abbas W. MRI induced heating of artificial bone implants. *Journal of Electromagnetic Waves and Applications*. 2009;**23**:799-808
- [29] Li D, Zheng J, Liu Y, et al. An efficient approach to estimate MRI RF field induced in vivo heating for small medical implants. *IEEE Transactions on Electromagnetic Compatibility*. 2015;**57**(4):643-650
- [30] Zheng J, Li D, Chen J, et al. Numerical study of SAR for multi-component orthopaedic hip replacement system during MRI. *Electromagnetic Compatibility (EMC), 2016 IEEE International Symposium on IEEE*, 2016: 116-120

- [31] Zeng Q, Wang Q, Zheng J, et al. MRI induced heating for fully implanted, partially implanted and minimally implanted medical electrode leads. *Electromagnetics in Advanced Applications (ICEAA), 2015 International Conference on IEEE, 2015*: 1590-1591
- [32] Zeng Q, Zheng J, Chen J. MRI Induced heating for fully implanted, partially implanted and minimum implanted medical electrode leads. *Applied Computational Electromagnetics (ACES), 2015 31st International Review of Progress in IEEE, 2015*:1-2
- [33] Hand JW. Modelling the interaction of electromagnetic fields (10 MHz–10 GHz) with the human body: Methods and applications. *Physics in Medicine and Biology*. 2008;**53**(16):R243
- [34] Andreo P. Monte Carlo techniques in medical radiation physics. *Physics in Medicine and Biology*. 1991;**36**(7):861
- [35] Yee K. Numerical solution of initial boundary value problems involving Maxwell's equations in isotropic media. *IEEE Transactions on Antennas and Propagation*. 1966;**14**(3): 302-307
- [36] Patankar SV. *Numerical Heat Transfer and Fluid Flow*. New York: Hemisphere; 1980. p. 25-73
- [37] Christ A, Kainz W, Hahn EG, et al. The virtual family—Development of surface-based anatomical models of two adults and two children for dosimetric simulations. *Physics in Medicine and Biology*. 2009;**55**(2):N23